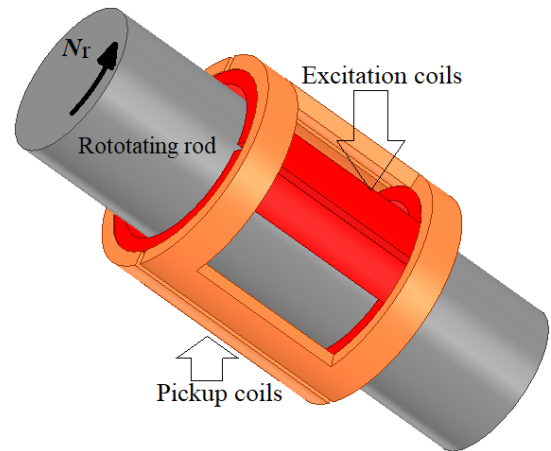


# 3D Analytical Modeling of Rotational Eddy Current Speed Sensor

Mehran Mirzaei, and Pavel Ripka

Faculty of Electrical Engineering, Czech Technical University, 16627, Prague, Czech Republic  
([mirzameh@fel.cvut.cz](mailto:mirzameh@fel.cvut.cz), [Ripka@fel.cvut.cz](mailto:Ripka@fel.cvut.cz)).

**Abstract**—The main goal of this paper is to present a novel 3D analytical method for precise and fast modeling of rotational eddy current speed sensors with cylindrical structures. An equivalent linearized model is developed using a multi-slice structure. The cylindrical structure of rotational eddy current sensors is modeled using the multi-slice linearized structure. The 3D distribution of induced eddy current in the rotating conductive rods is considered in the analytical modeling. The method of separation of variables using Fourier series is utilized for the analytical analysis of rotational eddy current speed sensors. The new calculation method was tested on eddy current speed sensor with perpendicular coils with different rotating rods. The analytical results are compared with the calculations of 3D time harmonic and time stepping finite element methods. The measurements on the sensor prototypes verified the calculations. The 3D analytical method. Compared with 3D Time Harmonic FEM, the 3D analytical method is 12-times faster



**Index Terms**—3D analytical method, Fourier series, eddy current analysis, measurement, rotational speed sensor.

## I. Introduction

THE measurement and estimation of rotating speed of moving objects is critical for automation and robotic applications. The induction machines have cost-effective, simple, and robust rotors and high performance, which make them the best options for various industrial applications [1]. Induction machines with light rotors are the best option for fast servo systems [2], despite their lower efficiency in comparison with permanent magnet machines [3]. They can have a totally nonmagnetic light rotor and rotating part for fast tracking [4]. Accurate speed measurement is required for optimum operation of induction machines at different loading conditions.

Using sensorless method to estimate the speed of rotating induction machines has been well developed in recent years [1], which is a nondestructive and contactless nonphysical approach. However, it endures from its complicated hardware used for signal processing, susceptibility to electrical faults in the stator windings, and insufficient fast response at dynamic conditions. Physical speed sensors using encoders and resolvers [5]-[6] are commonly used for speed measurement in rotating machinery. Installing their moving parts on the rotating rods and shafts makes them vulnerable to mechanical faults and high vibrations, which affect the accuracy of the speed measurement.

The motional component of induced eddy current in solid,

conductive moving objects is used for contactless speed measurement systems with a cost-effective and robust structure [7]-[9]. Rotational eddy current sensors have shown appropriate performance for speed measurement based on the differential voltage structure in [10] and the differential flux linkage structure in [11]. They are contactless and simple, which makes them attractive for industrial applications. .

The design and performance analysis of rotational eddy current sensors require computational tools. The 2D analytical method [11] and the 2D finite element method (FEM) are suitable tools for fast analysis. However, precise modeling of the 3D distribution of induced eddy current in the rotating rod is impossible in 2D analysis. 3D FEM is preferred in terms of accuracy. The motional induced current using Minkowski transformation can be modeled in 3D FEM with a fixed mesh for smooth moving conductive objects [12]-[13]. However, it has numerical oscillations if the local Peclet number [12] exceeds 2, and it requires complicated upwinding techniques to remove the numerical oscillations in the FEM simulations [12], [14]-[17] or decreasing mesh sizes. In such case, the simulation time will significantly increase, and a larger memory will be required. An alternative approach to modeling motional induced eddy current is direct modeling of motion using two meshes with a time stepping approach. They correspond to the fixed part and moving parts, which are coupled using Lagrange surfaces [13],

sliding mesh approaches [18]-[19] or an inner layer with varying mesh. The main disadvantage of time stepping FEM is the long simulation time and the non-useful transient part of the simulation. A time-periodic approach can be used to reduce the transient part of simulation, as steady state results are required for the analysis and design of electromagnetic devices and sensors [20]-[21]. However, these techniques are not sufficient to reduce significantly the simulation time of eddy current speed sensors. Implementing a 3D analytical method with consideration of motion and induced eddy currents is the best alternative approach to the time consuming and complicated 3D FEM [5]-[6].

Linearization of cylindrical and disc shape magnetic devices has been used to simplify 3D analytical calculations [22] and solve differential equations in Cartesian coordinates [23]. However, this method can cause large errors if the rotating part in the cylindrical structure has a considerably smaller diameter than the stationary part and the curvature angle of the coils is greater than 60 deg. A multi-slices model could be used to solve analytically governing differential equations in Cartesian coordinates and avoid complexity of 3D solving of differential equations in cylindrical coordinates [24]-[26]. The multi-slice approaches presented in [24]-[26] are used only for disc shape induction motors, so that these are quasi-3D calculations and not fully 3D modeling of magnetic fields and induced eddy currents.

A novel 3D analytical method is developed to model the eddy current speed sensor using a multi-slice approach for the cylindrical magnetic structures. The 3D analytical method is demonstrated and verified on eddy current speed sensor with two excitation and perpendicular pickup coils. The sensor, rotating rod, and surrounding air are divided into circular slices of adequate thickness. The field calculations are performed in each slice in Cartesian coordinates. The 3D analytical results of the eddy current speed sensor are compared with 3D time harmonic and time stepping FEM results and measurements on sensor demonstrator at different speeds and excitation frequencies.

## II. MODELLING

### A. Structure

The 3D structure of the eddy current sensor is shown in Fig. 1 a) with a rotating rod with speed,  $N_r$ . The sensor includes double-saddle inner and outer coils [11]. Either inner or outer coils can be used as excitation coils or pickup coils, according to the reciprocity theorem. In this paper, the inner coils are considered excitation coils, and the outer coils are pickup coils. The excitation and pickup coils are perpendicularly located, as shown in Fig. 1 a) and Fig. 2. The winding directions in the excitation and pickup coils are shown in Fig. 2.

A perpendicular configuration of excitation and pickup coils causes zero induced voltage in the pickup coils at zero speed of the conductive rod when the excitation coils are connected to an AC electrical source. The pickup coils sense zero flux linkage at zero speed as the magnetic flux generated by the excitation coils current is symmetric. When the rod rotates, voltage is induced into the pickup coils [11] due to the asymmetric magnetic flux distribution caused by the motional component of induced currents in the rotating rod. This phenomenon can be used for rotating speed measurement.

The structural parameters of the sensor and rotating rod are shown in Fig. 1 a) and Fig. 2. The parameter  $L_c$  is inner axial length of the sensor coils in Fig. 1 a).  $r_r$  is the outer radius of the rotating rod. The parameters,  $r_{ei}$ ,  $r_{eo}$ ,  $r_{pi}$  and  $r_{po}$  are the inner and outer radii of the excitation coils and inner and the outer radii of the pickup coils, respectively. The parameters,  $\theta_{ei}$ ,  $\theta_{eo}$ ,  $\theta_{pi}$  and  $\theta_{po}$  are the inner and outer span angles of the excitation coils and the inner and outer span angles of the pickup coils, respectively.

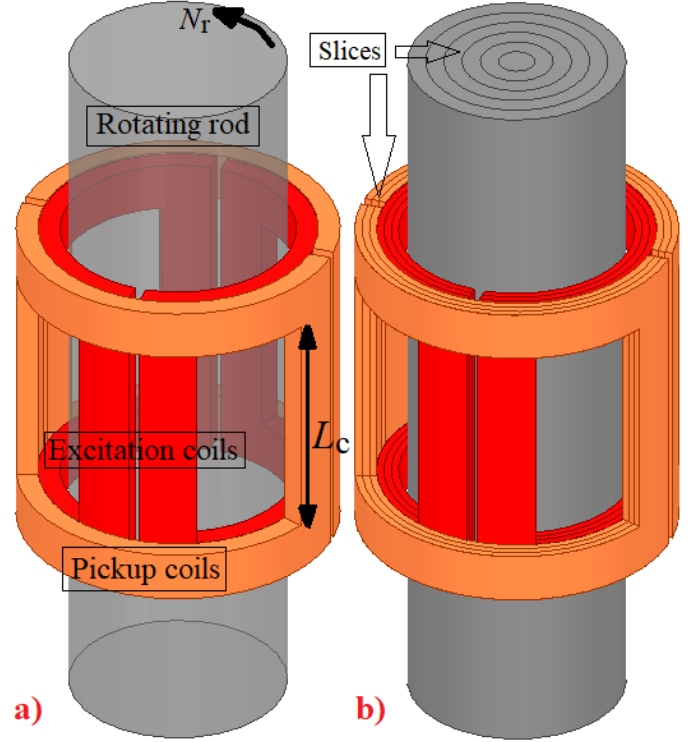


Fig. 1. Eddy current speed sensor, a) 3D model, b) 3D sliced model of eddy current speed

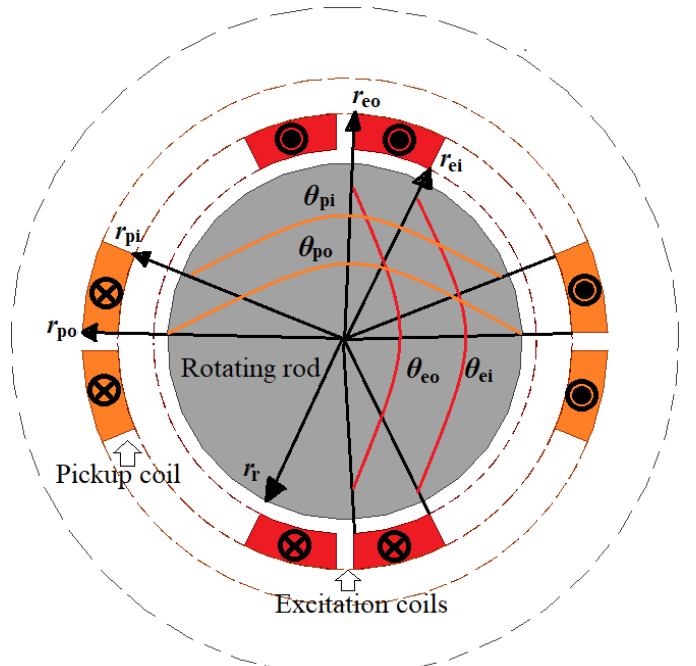


Fig. 2. A 2D cross sectional view of eddy current speed sensor

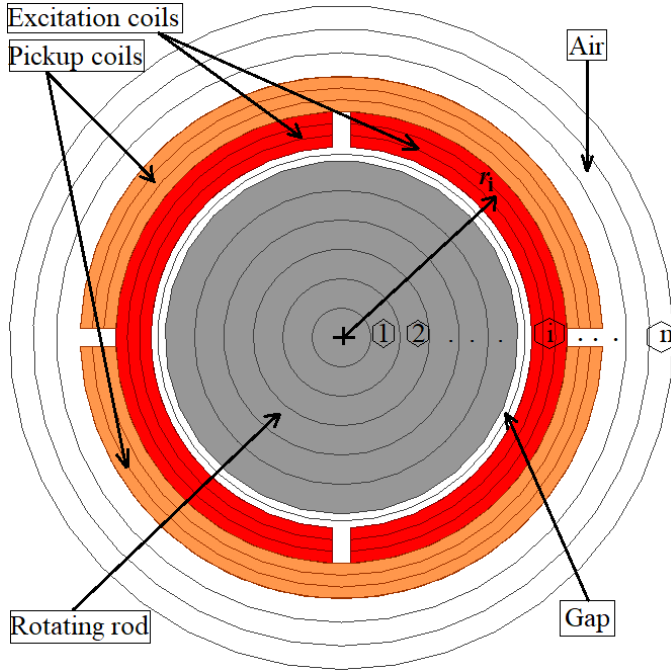


Fig. 3. 2D cross sectional view of sliced model of rotational eddy current speed sensor.

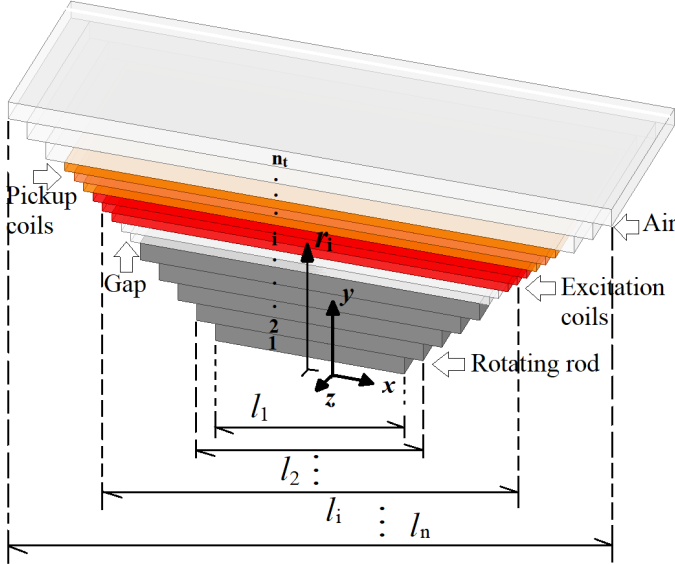


Fig. 4. 3D view of linearized model of rotational eddy current speed sensor.

### B. 3D Analytical Calculations

The multi-slice method is used to obtain the magnetic fields of the rotational eddy current speed sensor. The sensor coils, rotating rod, and surrounding air regions are divided into multiple slices and layers, as shown in Fig. 1 b) and Fig. 3. The linearized structure of each slice of sensor parts is shown in Fig. 4. The numbers of slices are  $n_r$ ,  $n_g$ ,  $n_e$ ,  $n_p$  and  $n_a$  for the rotor part, the gap part between the rotor and excitation coils, the excitation coils part, the pickup coils part, and the air part beyond the coils, respectively. Therefore, the total number of slices in the model is  $n_t = n_r + n_g + n_e + n_p + n_a$ . The parameter,  $r_i$  in Fig. 4 is the radius of the layer,  $i$ . The outer radius of the air region beyond the coils in Fig. 3 is selected to be large enough to apply the tangential field or zero normal field boundary conditions. The parameters,

$l_1, l_2, \dots, l_i, \dots, l_n$  are the mean azimuthal lengths of layers in Fig. 4.

The Cartesian coordinates are utilized for the magnetic field analysis of the sensor. The currents of the excitation coils are flowing in  $x$ - and  $z$ -directions in the linearized model. Therefore, only the  $x$ - and  $z$ -components of magnetic vector potentials,  $A_{x,i}$ ,  $A_{z,i}$  are considered, and the  $y$ -component of magnetic vector potential,  $A_{y,i}$  is ignored. The differential equation in (1) is obtained using Coulomb gauge versus the  $z$ -component of magnetic vector potential,  $A_{z,i}$  for layer  $i$  and extracted from Maxwell equations [23]. A similar differential equation versus  $A_{x,i}$  can be obtained.

$$\frac{\partial^2 A_{z,i}}{\partial x^2} + \frac{\partial^2 A_{z,i}}{\partial y^2} + \frac{\partial^2 A_{z,i}}{\partial z^2} = -\mu_0 \mu_{r,i} \cdot J_{z,i} \quad (1)$$

(1)

$$\frac{\partial A_{x,i}}{\partial x} + \frac{\partial A_{z,i}}{\partial z} = 0 \quad (2)$$

(2)

where,  $\mu_{r,i}$  is relative magnetic permeability.

The  $z$ -component of current density,  $J_{z,i}$  in (1), is presented in (3) for the region of the conductive rod, in (4) for the excitation coils region, and in (5) for the current free regions of the air and pickup coils.  $f$ ,  $N_e$ , and  $I$  are the frequency, number of turns in each excitation coil, and rms value of the current in the excitation coils.

$$J_{z,i} = J_{z,i,t} + J_{z,i,m}$$

$$J_{z,i,t} = \sigma_i j \omega A_{z,i}, \quad J_{z,i,m} = \sigma_i V_i \frac{\partial A_{z,i}}{\partial x}$$

$$\omega = 2\pi f, \quad V_i = r_i \cdot 2\pi \frac{N_r}{60}$$

(3)

$$J_{z,i} = J_s, \quad J_s = \frac{N_e \cdot \sqrt{2} I}{\frac{r_{eo}^2 - r_{ei}^2}{2} \cdot \frac{\theta_{eo} - \theta_{ei}}{2}}$$

(4)

$$J_{z,i} = 0 \quad (5)$$

(5)

The induced eddy current in the rotor has two components: 1: transformer component caused by time-varying source magnetic field,  $J_{x,z,i,t}$  2: motional component caused by relative motion between conductive rod and source field,  $J_{x,z,i,m}$  with linear speed  $V_i$  in (3) corresponding to each layer of the linearized model.

The method of separation of variables using Fourier series is used to analytically solve the differential equation in (1). The solutions for  $A_{x,i}$  and  $A_{z,i}$  are presented in (6) using (7) and (8).  $m$  and  $n$  are harmonic orders in the Fourier series.

$$A_{z,i} = \sum_m \sum_n A_i^{m,n} \cdot e^{j(\omega t - p_i x - q_i z)}$$

$$A_{x,i} = \sum_m \sum_n \frac{q_i}{p_i} A_i^{m,n} \cdot e^{j(\omega t - p_i x - q_i z)}$$

(6)

$$p_i = m \frac{\pi}{l_i}, \quad m = \pm 1, \pm 3, \dots, \quad q_i = n \frac{\pi}{L}, \quad n = \pm 1, \pm 3, \dots \quad (7)$$

(7)

$$(8) \quad A_i^{m,n} = C_{1,i} \cdot e^{\gamma_i(y-r_i)} + C_{2,i} \cdot e^{-\gamma_i(y-r_i)} + \alpha_i$$

The axial length  $L$  in (7) is selected for Fourier series analysis, which should be large enough to apply the tangential field or zero normal field boundary conditions. The parameter  $\gamma_i$  in (8) is presented in (9) for the rotating rod region and in (10) for other regions.

$$(9) \quad \gamma_i = \sqrt{p_i^2 + q_i^2 + j\sigma_i\mu_0\mu_{r,i}(\omega - V_i \cdot p_i)}$$

$$(10) \quad \gamma_i = \sqrt{p_i^2 + q_i^2}$$

The equation (11) is used for the parameter  $\alpha_i$  in (8) for the excitation coils region, and the equality in (12) is used for other regions.

$$(11) \quad \alpha_i = \mu_0 \cdot \frac{J_{e,i}}{p_i^2 + q_i^2}$$

$$(12) \quad \alpha_i = 0$$

The parameter  $J_{e,i}$  in (11) is calculated in (13) corresponding to the 2D linearized model of excitation coils shown in Fig. 5 a) using dimensional parameters in (14).

$$(13) \quad \begin{aligned} C_{e,i} &= 4 \frac{j}{n\pi l_i} \cdot \left( \frac{1}{p_i + q_i} C_{e,i-1} - \frac{1}{p_i - q_i} C_{e,i-2} \right) \\ C_{e,i-1} &= \cos\left(p_i \frac{w_{e,i} + t_{e,i}}{2} + q_i \frac{L_c + t_{e,i}}{2}\right) \cdot \sin\left(p_i \frac{t_{e,i}}{2} + q_i \frac{t_{e,i}}{2}\right) \\ C_{e,i-2} &= \cos\left(p_i \frac{w_{e,i} + t_{e,i}}{2} - q_i \frac{L_c + t_{e,i}}{2}\right) \cdot \sin\left(p_i \frac{t_{e,i}}{2} - q_i \frac{t_{e,i}}{2}\right) \end{aligned}$$

$$(14) \quad w_{e,i} = r_i \cdot \theta_{ei}, \quad t_{e,i} = r_i \cdot \frac{\theta_{eo} - \theta_{ei}}{2}$$

where,  $w_{e,i}$  and  $t_{e,i}$  in (14) shown in Fig. 5 a) are the inner width and thickness of the excitation coils in  $i^{\text{th}}$  layer and slice.

The constants  $C_{1,i}$  and  $C_{2,i}$  in (8) are calculated using boundary conditions in (15) between layers and slices.  $B_{y,i}$  and  $H_{z,i}$  are the normal  $y$ -component of magnetic flux density and axial tangential  $z$ -component of magnetic field strength in each layer, respectively.

$$(15) \quad \begin{aligned} B_{y,1} \Big|_{y=r_1 - \frac{d_{r,1}}{2}} &= 0 \\ \vdots \\ r_i \cdot B_{y,i} \Big|_{y=r_i + \frac{d_{r,i}}{2}} &= r_{i+1} \cdot B_{y,i+1} \Big|_{y=r_{i+1} - \frac{d_{r,i+1}}{2}} \\ H_{z,i} \Big|_{y=r_i + \frac{d_{r,i}}{2}} &= H_{z,i+1} \Big|_{y=r_{i+1} - \frac{d_{r,i+1}}{2}} \\ \vdots \\ B_{y,n_t} \Big|_{y=r_{n_t} + \frac{d_{r,n_t}}{2}} &= 0 \end{aligned}$$

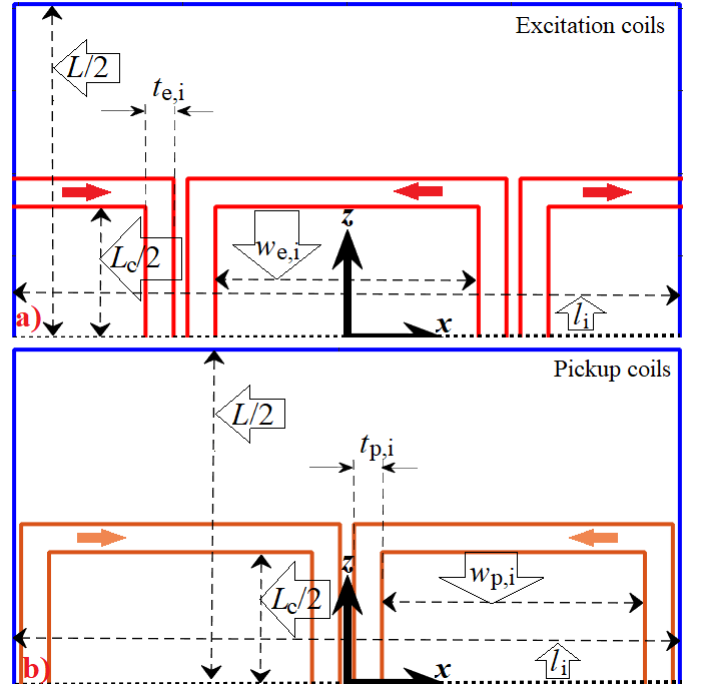


Fig. 5. Half of 2D model of linearized structure of the sensor coils in  $z$ - $x$  plane – The model is symmetric in axial  $z$ -direction

The induced voltage in the pickup coils  $U_p$  in (16), is calculated by the averaging of the calculated flux linkage,  $\Psi_{p,i}$  in (17) for  $n_p$  layers in the pickup coils region.

$$(16) \quad U_p = -j\omega \frac{1}{n_p} \sum_{i=n_r+n_g+n_e+1}^{n_r+n_g+n_e+n_p} \Psi_{p,i}$$

The flux linkage  $\Psi_{p,i}$  for  $i^{\text{th}}$  of the pickup coils region is calculated by surface and line integrations in (17). The surface integration is performed on the cross-sectional area,  $t_{p,i} \cdot d_{r,i}$  of the pickup coils for each layer. The line integration is carried out on the winding loop of the pickup coils region, whose winding direction is shown by arrows. The equation of  $\Psi_{p,i}$  is presented in (18) using the parameters of (19) and (20).  $N_p$  is the number of turns in each pickup coil, and  $d_{r,i}$  is the radial thickness of each layer shown in Fig. 3 and Fig. 4.

$$(17) \quad \Psi_{p,i} = \frac{N_p \iint A_{x,z,i} \cdot dl \, ds}{t_{p,i} \cdot d_{r,i}}$$

$$(18) \quad \begin{aligned} \Psi_{p,i} &= -2j \frac{N_p \cdot L \cdot l_i}{n_p \cdot t_{p,i} \cdot d_{r,i}} \sum_m \sum_n \left( 1 + \frac{q_i^2}{p_i^2} \right) \cdot U_i \cdot C_{p,i} \cdot \sin\left(p_i \frac{l_i}{2}\right) \\ U_i &= \frac{(C_{1,i} + C_{2,i})}{\gamma_i} 2 \sinh\left(\gamma_i \frac{d_{r,i}}{2}\right) \end{aligned}$$

$$\begin{aligned} C_{p,i} &= 4 \frac{j}{n\pi l_i} \cdot \left( \frac{1}{p_i + q_i} C_{p,i-1} - \frac{1}{p_i - q_i} C_{p,i-2} \right) \\ C_{p,i-1} &= \cos\left(p_i \frac{w_{p,i} + t_{p,i}}{2} + q_i \frac{L_c + t_{p,i}}{2}\right) \cdot \sin\left(p_i \frac{t_{p,i}}{2} + q_i \frac{t_{p,i}}{2}\right) \\ C_{p,i-2} &= \cos\left(p_i \frac{w_{p,i} + t_{p,i}}{2} - q_i \frac{L_c + t_{p,i}}{2}\right) \cdot \sin\left(p_i \frac{t_{p,i}}{2} - q_i \frac{t_{p,i}}{2}\right) \end{aligned}$$



(19)

$$w_{p,i} = r_i \cdot \theta_{pi} \quad t_{p,i} = r_i \cdot \frac{\theta_{po} - \theta_{pi}}{2}$$

(20)

where,  $w_{p,i}$  and  $t_{p,i}$  in (17)-(20) shown in Fig. 5 b) are the inner width and thickness of the pickup coils in  $i^{\text{th}}$  layer and slice.

### III. THE 3D ANALYTICAL RESULTS IN COMPARISON WITH 3D FEM AND EXPERIMENTAL RESULTS

Fig. 6 and Fig. 7 show the experimental setup of the rotational eddy current speed sensor and its elements. Table I presents the parameters and dimensions of the eddy current speed sensor and rotating rod. Two nonmagnetic aluminum and copper rods are used for the analysis and measurement. The speed range is considered to be  $\pm 3000$  rpm.

TABLE I  
EDDY CURRENT SPEED SENSOR PARAMETERS

Par.		Par.	
$r_i$	15 mm	$\theta_{pi}$	135.2 deg.
$r_{ei}$	16.2 mm	$\theta_{po}$	175.8 deg.
$r_{eo}$	19.2 mm	$L_c$	32 mm
$r_{pi}$	19.2 mm	$\sigma_{Cu}$	56.66 MS/m
$r_{po}$	22.2 mm	$\sigma_{Al}$	20.97 MS/m
$\theta_{ei}$	127.5 deg.	$N_e$	100
$\theta_{eo}$	175.1 deg.	$N_p$	115

#### A. The Eddy Current and Magnetic Flux Distribution

Fig. 8 shows the eddy current distribution on the surface of a rotating aluminum rod using the 3D analytical method in the linearized structure at 3000 rpm, 500 Hz and 1250 Hz. The streamline function  $S$  in (21) and (22) is used to draw equi-values using contour plots in MATLAB. The eddy current distribution is more concentrated at higher frequencies because of higher reaction fields and skin effects.

$$\nabla \cdot J = 0 \rightarrow J = \nabla \times S, \quad S = (0, S_y, 0)$$

(21)

$$S_y(y = r_r) = \int J_z(y = r_r) dx = - \int J_x(y = r_r) dz =$$

$$\sigma_i \sum_m \sum_n \frac{(\omega - V_i \cdot p_i)}{p_i} A_i^{m,n}(y = r_r) \cdot e^{j(\omega t - p_i x - q_i z)}$$

$$A_i^{m,n}(y = r_r) = C_{1,i} \cdot e^{\gamma_i \frac{d_{r,i}}{2}} + C_{2,i} \cdot e^{-\gamma_i \frac{d_{r,i}}{2}}$$

(22)

Fig. 9 shows the magnetic flux distribution in the sensor using the equi-potential of the  $z$ -component of the magnetic vector potential,  $A_{z,i}$  in (23) on the middle plane of the sensor in the axial direction,  $z = 0$ , where the  $x$ -component of magnetic vector potential is zero,  $A_{x,i} = 0$ . The magnetic flux distribution is asymmetric due to the motional effect, which induces voltages in the pickup coils.

$$A_{z,i}(z = 0) = \sum_m \sum_n A_i^{m,n} \cdot e^{j(\omega t - p_i x)}$$

(23)

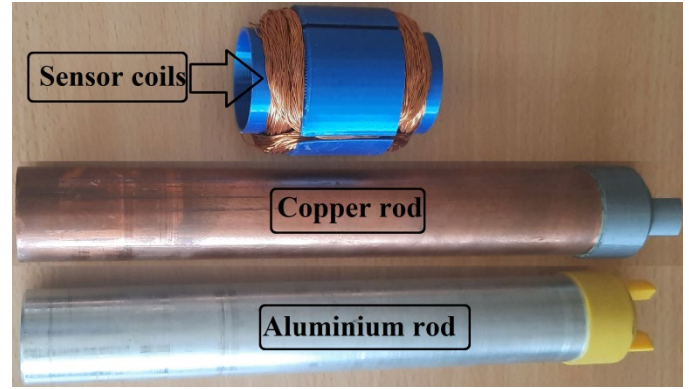


Fig. 6. The sensor coils, aluminium and copper rods.

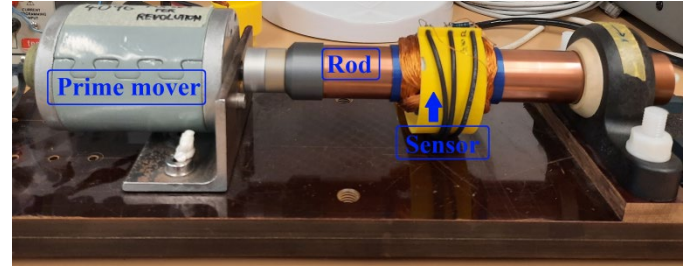


Fig. 7. The measurement setup for the rotational eddy current speed sensor.

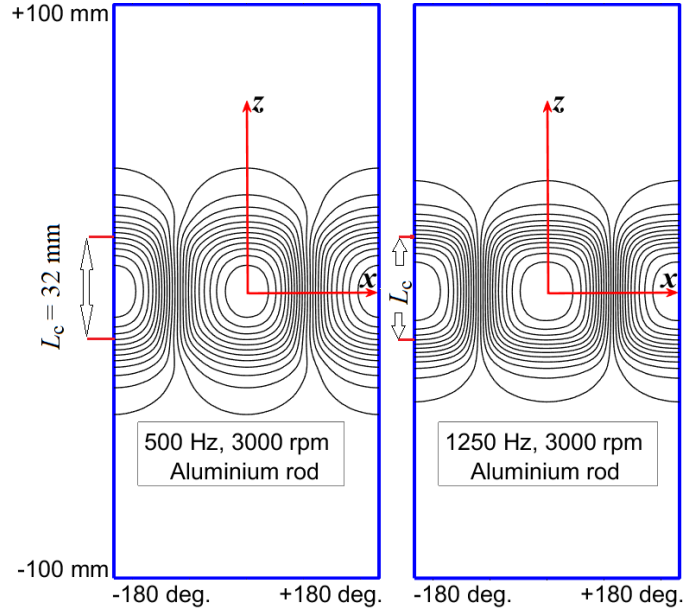


Fig. 8. Eddy current distribution on the surface of rotating rod in the linearized model – Aluminium rod, 500 Hz, 1250 Hz and 3000 rpm

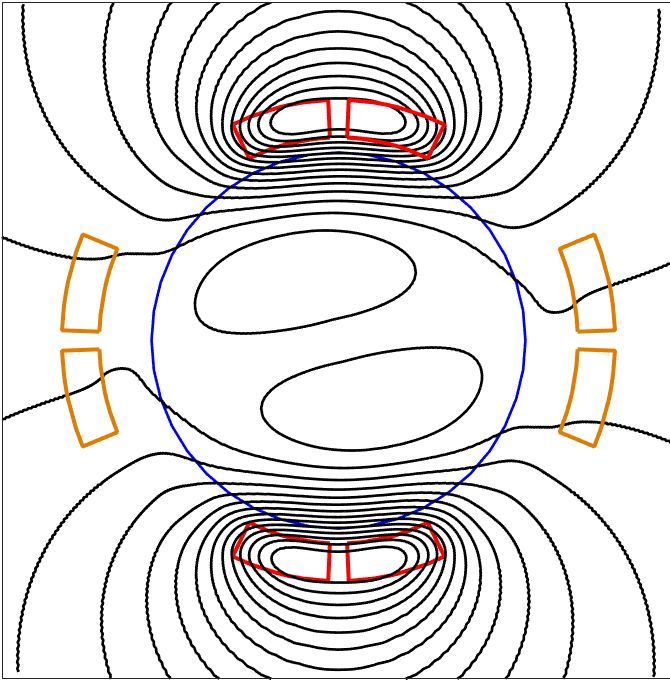


Fig. 9. 2D magnetic flux distribution in the mid-plane of the sensor and rotating rod at 500 Hz and 3000 rpm.

### B. Comparison between 3D Analytical and 3D FEM

Table II presents the comparison of the calculated inductances using 3D analytical and time harmonic FEM modeled in Ansys/Maxwell software with and without a rod (air). The 3D analytical method has excellent accuracy for inductance estimation, where the difference between 3D analytical and FEM results is 0.6% - 1.8%. The number of mesh elements in 3D time harmonic FEM is 233198. The simulation time is 1/12<sup>th</sup> for the 3D analytical method in comparison with the 3D time harmonic method. The values of parameters  $L = 400$  mm,  $n_r = 40$ ,  $n_g = 8$ ,  $n_e = 8$ ,  $n_p = 8$  and  $n_a = 200$  are selected for accurate simulation of 3D analytical modeling. The outer radius of the air region beyond the sensor coils is considered,  $r_o = 622.2$  mm. The maximum harmonic orders,  $m$  and  $n$  are selected 11 and 151, respectively.

TABLE II  
COMPARISON BETWEEN 3D ANALYTICAL AND 3D TIME HARMONIC FEM AND ELAPSED TIME – INDUCTANCE

0 rpm			3D FEM		3D Analytical	
			$L, \text{mH}$	Elapsed time	$L, \text{mH}$	Elapsed time
Air		Exc.	1.715	3 m, 27 s	1.704	17.4 s
		Pk.	2.578	3 m, 27 s	2.554	17.4 s
Al	500 Hz	Exc.	1.20	3 m, 27 s	1.181	17.4 s
		Pk.	2.076	3 m, 27 s	2.054	17.4 s
	1250 Hz	Exc.	1.026	3 m, 27 s	1.013	17.4 s
		Pk.	1.933	3 m, 27 s	1.915	17.4 s
Cu	500 Hz	Exc.	1.015	3 m, 27 s	1.001	17.4 s
		Pk.	1.923	3 m, 27 s	1.905	17.4 s
	1250 Hz	Exc.	0.897	3 m, 27 s	0.881	17.4 s
		Pk.	1.833	3 m, 27 s	1.813	17.4 s

The comparison between the calculated voltage-to-current ratio using the 3D analytical method and time stepping FEM is presented in Table III with a maximum difference error of 5.2%. The analytical and FEM simulations are presented for copper

and aluminium rods at 3000 rpm, 500 Hz and 1250 Hz. The rod motion is considered in the 3D time stepping FEM using Ansys/Maxwell software, which demands a fine mesh. The number of mesh elements in 3D time stepping FEM is 268895. The simulation time for 3D analytical modeling is only 3.6 s in comparison with several hours of 3D time stepping FEM simulations. The parameter  $L$  is selected 200 mm, and the maximum harmonic orders  $m$  and  $n$  are considered 11 and 31, respectively. The values of parameters  $n_r$ ,  $n_g$ ,  $n_e$ ,  $n_p$ ,  $n_a$ , and  $r_o$  used for the voltage calculations are the same as for the inductance calculations.

TABLE III  
COMPARISON BETWEEN 3D ANALYTICAL AND 3D TIME STEPPING FEM FOR SENSITIVITY CALCULATION: VOLTAGE TO CURRENT VALUES AND ELAPSED CALCULATION TIME

3000 rpm		3D FEM		3D Analytical	
		$U_p/I$	Elapsed time	$U_p/I$	Elapsed time
Al	500 Hz	51.6 mV/A (100%)	3 h, 4 m, 58 s	54.3 mV/A (105.2%)	3.6 s
	1250 Hz	31.6 mV/A (100%)	4 h, 51 m, 50 s	31.0 mV/A (98.1%)	3.6 s
Cu	500 Hz	30.0 mV/A (100%)	5 h, 31 m, 16 s	29.9 mV/A (99.7%)	3.6 s
	1250 Hz	20.1 mV/A (100%)	10 h, 55 m, 51 s	19.6 mV/A (97.5%)	3.6 s

### C. Comparison between 3D Analytical and Experiments

A lock-in amplifier is used to measure the sensor voltage at various speeds. Fig. 10 and Fig. 11 show the absolute value of voltage to current ratio versus speed for the aluminium and copper rods where the 3D analytical results are compared with the experimental results. 3D analytical results match well with the experimental results, which show appropriate accuracy of the new analytical results for different speeds, excitation frequencies and materials of rotating rods. The modeling of rotational eddy current is required to be performed for various speeds and excitation frequencies. Therefore, a lot of simulation time is saved using the 3D analytical method in comparison with 3D time stepping FEM.

The sensitivity of the sensor with an aluminium rod is about two times higher in comparison with a copper rod. Aluminum has 63% lower conductivity,  $\sigma_{Al} = 20.97$  MS/m in comparison with copper  $\sigma_{Cu} = 56.66$  MS/m, and therefore, the magnetic flux penetrates more into the rotating rod. Higher magnetic flux penetration increases the sensor sensitivity. The same phenomenon is shown with increasing frequency. It decreases the sensitivity because of the lower magnetic flux penetration caused by the stronger skin effect at higher frequencies. The 3D analytical method correctly estimates the sensor performance for different rod materials and excitation frequencies. High linearity in the measured curve of voltage versus speed is presented, which is also shown by 3D analytical results. Therefore, the eddy current sensor is a suitable transducer for rotating speed measurement and estimation. And 3D analytical method can be used for further detailed analysis and design optimization.

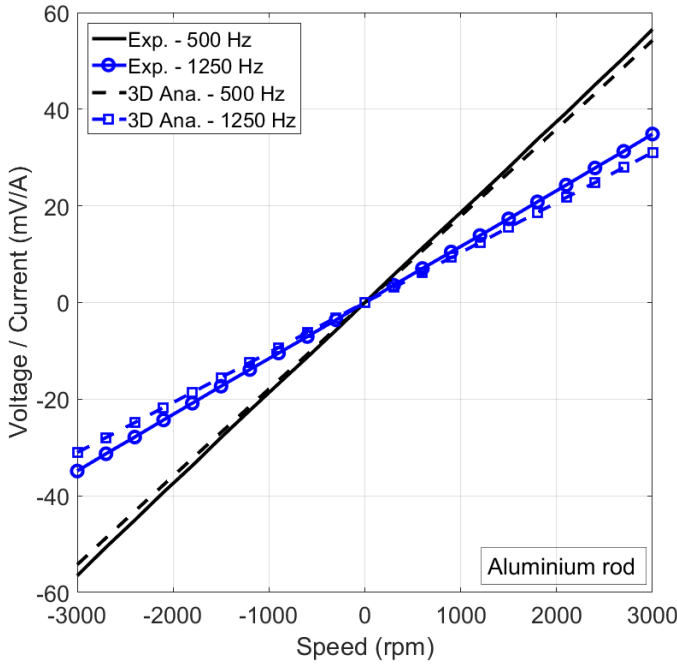


Fig. 10. The comparison of analytically calculated (3D Ana.) and measured (Exp.) voltage to current ratio versus speed for aluminium rod at 500 Hz and 1250 Hz.

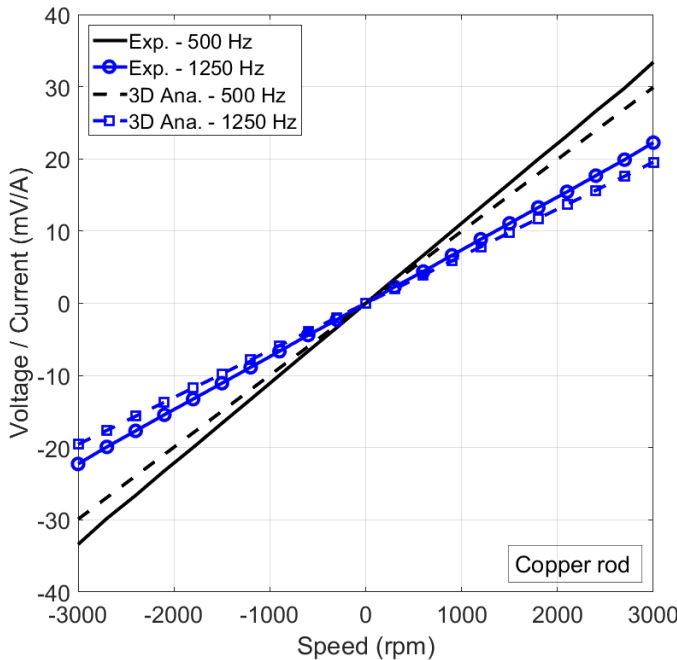


Fig. 11. The comparison of analytically calculated (3D Ana.) and measured (Exp.) voltages to current ratio versus speed for copper rod at 500 Hz and 1250 Hz.

#### IV. CONCLUSION

A novel 3D analytical method was presented for fast and accurate analysis of a rotational eddy current speed sensor with a cylindrical structure. The analytical results of the inductances of the sensor coils and the induced voltage in the pickup coils are compared with 3D FEM calculations and measurements to evaluate the accuracy of the 3D analytical method.

Two nonmagnetic aluminium and copper rods are used for the analysis and measurement to assess material effects of the rotating rod. The presented 3D analytical method is general and can be

used for other structures of excitation and pickup coils and ferromagnetic iron rods, taking into account the relative magnetic permeability of iron.

Short-time simulations using the proposed 3D analytical method with appropriate accuracy help with the fast analysis and design optimization of rotational eddy current speed sensors. It avoids using time-consuming 3D FEM modeling and costly software for parametric analysis and design optimization of the sensor.

#### ACKNOWLEDGMENT

We thank Dr. Vaclav Grim for his support in performing measurements and manufacturing the experimental setup.

#### REFERENCES

- [1] C. J. Schantz and S. B. Leeb, "Self-sensing induction motors for condition monitoring," *IEEE Sensors J.*, vol. 17, no. 12, pp. 3735-3743, June 2017
- [2] B. V. Jayawant and P. J. Parr, "Sleeve-rotor induction motors for control applications," *IEEE Trans. Power Apparatus & Systems*, vol. 88, no. 7, pp. 1103 - 1114, July 1969
- [3] T. Noguchi and K. Fujita, "Electrical and mechanical compatible design of 15 kW, 150,000 r/min ultra-high-speed PM motor," *2019 22nd International Conference on Electrical Machines and Systems (ICEMS)*, Harbin, China, 11-14 August 2019
- [4] O. Bottauscio, F. Casaro, M. Chiampi, S. Giors, C. Maccarrone, and M. Zucca, "High-Speed Drag-Cup Induction Motors for Turbo-Molecular Pump Applications," *IEEE Trans. Magnetics*, vol. 42, no. 10, pp. 3449-3451, Oct. 2006
- [5] A. Paymoud, H. Saneie, Z. Nasiri-Gheidari, and F. Tootoonchian, "Subdomain model for predicting the performance of linear resolver considering end effect and slotting effect," *IEEE Sensors J.*, vol. 24, pp. 1447-14755, Dec. 2020
- [6] F. Zare and Z. Nasiri-Gheidari, "Magnetic equivalent circuit model for predicting performance of 2DOF wound rotor resolver," *IEEE Sensors J.*, vol. 21, no. 19, pp. 21417-21424, Oct. 2021
- [7] T. Itaya, K. Ishida, A. Tanaka, and N. Takehira, "Exact analysis of a linear velocity sensor," *IEEE Trans. Inst. & Meas.*, vol. 70, 6002106, 2021
- [8] A. Onat and S. Markon, "Theoretical and Experimental Analysis of Eddy Current Contactless Speed Sensors for Linear Motor Elevators," *IEEE Sensors J.*, vol. 22, no. 7, pp. 6345 - 6352, 2022
- [9] B. Feng, K. Deng, L. Xie, S. Xie, and Y. Kang, "Speed measurement method for moving conductors based on motion-induced eddy current," *IEEE Trans. Inst. & Meas.*, vol. 72, 6005608, 2023
- [10] M. Mirzaei, P. Ripka, V. Grim and A. Chirtsov, "Design and optimization of an eddy current speed sensor for rotating rods", *IEEE Sensors J.*, vol. 20, no. 20, pp. 12241-12251, Jun. 2020.
- [11] M. Mirzaei, P. Ripka, and V. Grim, "A Novel Structure of an Eddy Current Sensor for Speed Measurement of Rotating Shafts", *IEEE Trans. Energy Conversion*, vol.38, no.1, pp.170-179, 2023.
- [12] K.J. Binns, P.J. Lawrenson and C.W. Trowbridge, *The Analytical and Numerical Solutions of Electric and Magnetic Fields*, U.K., Wiley, 1992.
- [13] D. Rodger, "Modeling movement in electrical machines", *IEEE Trans. Magn.*, vol. 57, no. 6, Jun. 2021.
- [14] S. L. Ho, Y. Zhao, and W. N. Fu, "A characteristic Galerkin method for eddy-current field analysis in high-speed rotating solid conductors," *IEEE Trans. Magnetics*, vol. 48, no. 11, pp. 4634-4637, Nov. 2012
- [15] T. Furukawa K. Komiya, and I. Muta, "An upwind Galerkin finite element analysis of linear induction motors," *IEEE Trans. Magnetics*, vol. 26, no. 2, pp. 662 - 665, March 1990
- [16] S. Niikura and A. Kameari, "Analysis of eddy current and force in conductors with motion," *IEEE Trans. Magnetics*, vol. 28, no. 2, pp. 1450-1453, March 1992
- [17] E. K. C. Chan and S. Williamson, "Factors influencing the need for upwinding in two-dimensional field calculation," *IEEE Trans. Magnetics*, vol. 28, no. 2, pp. 1611-1614, March 1992
- [18] P. Zhou, Z. Badics, D. Lin and Z. J. Cendes, "Nonlinear T-Ω formulation including motion for multiply connected 3-D problems", *IEEE Trans. Magn.*, vol. 44, no. 6, pp. 718-721, Jun. 2008.

- [19] C. Lu, P. Zhou, D. Lin, B. He and D. Sun, "Multiply connected 3-D transient problem with rigid motion associated with T- $\Omega$  formulation", *IEEE Trans. Magn.*, vol. 50, no. 2, 7011004, Feb. 2014.
- [20] Y. Takahashi, T. Tokumasu, A. Kameari, H. Kaimori, M. Fujita, T. Iwashita, and S. Waka, "Convergence Acceleration of Time-Periodic Electromagnetic Field Analysis by the Singularity Decomposition-Explicit Error Correction Method," *IEEE Trans. Magnetism*, vol. 46, no. 8, pp. 2947-2950, Aug. 2010
- [21] H. Katagiri, Y. Kawase, and T. Yamaguchi, "Novel simplified time periodic-explicit error correction method for steady state analysis of AC magnetic field including DC component," *IEEE Trans. Power and Energy*, vol. 133, no. 3, pp. 271-276, 2013
- [22] E. Mendrela, J. Fleszar and E. Gierczak, *Modeling of Induction Motors With One and Two Degrees of Mechanical Freedom*, New York, NY, USA::Springer, 2003.
- [23] M. Mirzaei, P. Ripka, and V. Grim, "A linear eddy current speed sensor for speed measurement of magnetic and nonmagnetic conductive objects," *IEEE Trans. Ind. Appl.*, vol. 58, no. 6, pp. 7847-7856, 2022
- [24] H. Weh, H. Mosebach, and H. May "Analysis and characteristics of the disk-rotor induction machine", *Electr. Mach. Electromech.*, vol. 1, no. 1, pp. 87-98, 1976.
- [25] C. Hong, W. Huang and Z. Hu, "Performance calculation of a dual stator solid rotor axial flux induction motor using the multi-slice and multi-layer method", *IEEE Trans. Magn.*, vol. 55, no. 2, 8100709, Feb. 2019.
- [26] C. Hong, W. Huang, and Z. Hu, "Design and analysis of a high-speed dual stator slotted solid-rotor axial-flux induction motor," *IEEE Trans. Transportation Electrification*, vol. 5, no. 1, pp. 71-79, March 2019